From Collisions to Bundles: An Adaptive Coarse-Grained Model for the Aggregation of High-Aspect Ratio Carbon Nanotubes

Nikolaos Kateris,[†,¶] Philipp Kloza,[‡,¶] Rulan Qiao,[†] James A. Elliott,[*,‡] and Adam M. Boies[*,†]

†*Department of Engineering, University of Cambridge, Cambridge*
‡*Department of Materials Science and Metallurgy, University of Cambridge, Cambridge*
¶*Contributed equally to this work*

E-mail: jae1001@cam.ac.uk; a.boies@eng.cam.ac.uk

Phone: +44 (0)1223 335987; +44 (0)1223 746972

Abstract

We present an adaptive mesoscale model for carbon nanotube (CNT) systems. In our model, CNTs are represented as a chain of nodes connected by tensile and torsion springs to describe stretching and bending of the chain with intermolecular interactions being calculated using a mesoscopic Lennard-Jones potential. Computational adaptivity was achieved by dynamically adjusting node spacing and number during the simulation to optimise the number of simulated particles and lower computational effort. Adaptive simulations were up to five times faster than non-adaptive ones whilst quantitatively preserving all system dynamics. In particular, the model enables the study of the timescale of CNT bundling that leads to the formation of dilute CNT networks, so-called aerogels. These aerogels constitute the first step in the direct spinning of CNT fibres from chemical vapour deposition synthesis. Understanding the factors governing CNT bundling and network formation is key to controlling CNT fibre microstructure, and therefore optimising their properties. Using the model, we simulated the bundling dynamics of two CNTs with an initial point contact at varying angles for CNT lengths of up to $10\,\mu$m. We find that bundling times are an increasing function of initial collision angle and follow a power law with increasing CNT length that range from 10^{-1} to 10^{3} ns. We postulate that when this bundling time becomes of the same order as the CNT bundle collision time, the aerogel will form.

Introduction

Chemical vapour deposition (CVD) processes are the most common method of high-volume carbon nanotube (CNT) production[1] due to their scalability and simplicity. Among CVD processes, the floating catalyst chemical vapour deposition (FCCVD) process is of considerable academic and industrial interest for bulk CNT material production, as it produces a self-assembled macroscopic CNT aerogel which refers to dilute networks of CNTs. The FCCVD process allows single step production by combining nucleation, growth and aggregation of CNTs to form a hierarchical aerogel consisting of CNTs formed into bundles, and bundles

interconnected within the aerogel. The aerogel of continuous CNT fibres is extracted from the CVD system and is continuously wound up. Its main disadvantages have been the low density of reaction, requiring large reactor volumes for relatively low production rates,[2] as well as the presence of impurities. However, recent optimisation has greatly reduced impurities and their resulting effects.[3] Therefore developing an understanding of how the aerogel forms is critical in further process intensification and macroscopic property manipulation.
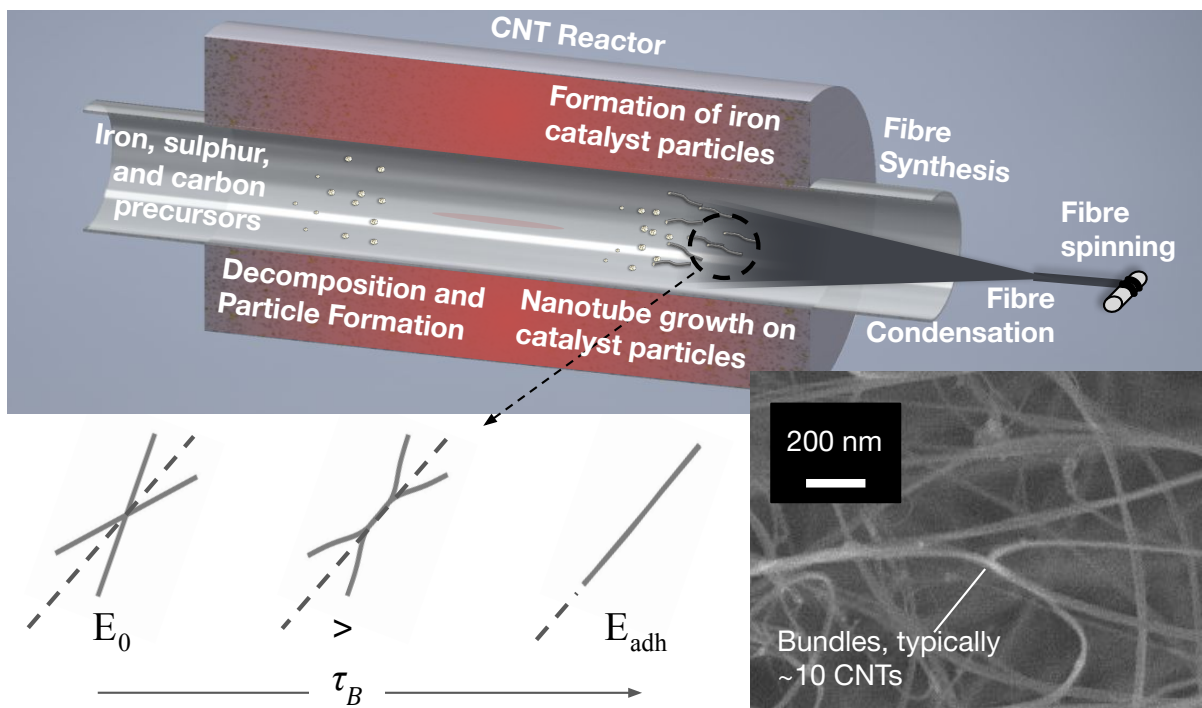

Figure 1: The phenomena occuring in the FCCVD process. Iron, sulphur and carbon precursors decompose to form catalyst nanoparticles, on which individual CNTs grow. They subsequently collide and reorient to form bundles. Bundle collisions lead to the formation of the CNT aerogel, which is subequently spun into CNT fibre. The bundles found in the aerogel typically consist of around 10 CNTs. In order to determine the bundling time τ_B, the intermolecular energy E of the CNT pair is used as a metric that indicates the completion of bundling.

The FCCVD process was initially developed by the Macromolecular Materials Laboratory at the University of Cambridge[4] and a schematic of the process, as well as scanning electron microscope images of the product are shown in Figure 1. The figure provides an overview of the process, which provides the context for this work. The reaction occurs in a hydrogen-

filled cylindrical furnace in the $1000\,°\mathrm{C}$ to $1300\,°\mathrm{C}$ temperature range. Methane, ferrocene, and thiophene are continuously injected into the furnace and decompose to form carbon and sulphur precursors as well as catalyst nanoparticles, on which individual CNTs grow. The CNTs undergo collisions which are governed by the thermal diffusion of the CNTs within the furnace and the corresponding collision kernel has recently been determined.[5] After collision, the intermolecular attractive van der Waals (vdW) forces cause the molecules to align and agglomerate into bundles. This process is illustrated on the lower left corner of Figure 1, where two individual CNTs align themselves, lowering their intermolecular energy from an initial value of E_0 to form a bundle with a final adhesion energy E_{adh} over a bundling time τ_{B}. It is experimentally observed that these bundles consist of about 3-20 close-packed CNTs and may be considerably longer than the individual CNTs.[5] Subsequently, the bundles collide and entangle to form a network of bundles, which is then drawn out of the furnace as fibre spun on a rotating drum, or as CNT sheets. The process of a dilute CNT aerosol to gel transition is referred to as a CNT aerogel in line with work for gas-phase spherical aggregates[6] and colloidal sol-gel systems.

Further understanding of the physical phenomena occurring in the FCCVD process is key to obtaining the desired CNT product and optimising and scaling the process further. Therefore, recent work has focused on theoretically, computationally, and experimentally investigating the principles governing the steps indicated in Figure 1.[2,7,8] The decomposition of chemical precursors and nucleation and growth of nanoparticles has been explored.[9] It was observed that catalyst nanoparticles nucleate, grow, in some cases disappear, and re-nucleate in the reactor, which affects the aerogel formation. The effect of sulphur in the chemical precursors on catalyst particle dynamics has also been explored.[10] The influence of the carbon source and catalyst nanoparticles on CNT growth has also been investigated.[11] It has additionally been shown that CNT growth rate increases rapidly with furnace temperature.[12]

The CNT collision rate was recently investigated by Langevin Dynamics modelling of collisions of single and multi-joint rods, which represent individual CNTs.[5] The results were

4

shown to agree with previous work on agglomeration of arbitrarily shaped particles,[13–15] which extends collision kernel theory to account for the collisions of arbitrarily shaped particles. Apart from collision frequencies, the distributions of collision position and collision angle were investigated.

Modelling the dynamics after collision is an area that has not been investigated in depth. Identifying the timescales that govern the various phenomena of Figure 1 is vital for modeling the aerogelation process. More specifically, comparing the bundling timescale τ_B with the timescale of CNT collisions is necessary to understand the bundle and aerogel formation process. Due to the flexibility of CNTs when the aspect ratio is high, treating them as rigid rods is not appropriate. A useful technique that captures the critical properties of interacting molecules is a Molecular Dynamics (MD) simulation which tracks the motion of each carbon atom. In MD, the computational cost scales approximately linearly with the number of atoms, thus simulating CNTs, whose length can be of the order of $100\,\mu m$ or $1\,mm$ is too computationally expensive. MD has been extensively used in CNT research to calculate elastic[16,17] and thermal properties,[18] as well as interactions with interfaces.[19]

An alternative to MD simulations for larger molecules is a mesoscale model in which atoms are lumped into larger masses in order to reduce the number of degrees of freedom of the system. Bead-spring mesoscale models have been used to model polymers where each molecule is treated as a series of massive beads connected by massless springs. Bead-spring models were pioneered by Rouse and Zimm[20] to model long flexible polymer chains. They treated long polymer molecules as a series of masses, joined by Hookean springs. Bead-spring Brownian mesoscale models have had numerous applications for polymers, nucleotides, proteins, and even CNTs.[21–23] Buehler exploited this technique to investigate the mechanical behaviour of CNTs.[24] Due to the high bending stiffness of CNTs, his model included rotational springs at each bead and the bead spacing was kept small to capture the physics of the interaction of different chains. Thus, the use of a coarse-grained model for the prediction of the mechanical properties of CNT systems has been established. Volkov et al.[25,26] later

developed a mesoscopic interaction potential to model CNT-CNT interactions. Combining this interaction potential with a model similar to Buehler's provides a useful framework for CNT dynamics simulations. The computational cost again scales with the number of simulated particles in the system, which brings a limit to the lengths of CNTs that can be investigated efficiently.

Motivated by the need to understand and model the physical phenomena in the FCCVD process, this work focuses on investigating the bundling of CNTs in said process. We present a framework for simulation of CNT bundling for high aspect ratio CNTs with lengths exceeding $10\,\mu m$, which are not able to be modelled due to the high cost of other current modelling frameworks. The simulations involve the post-collision dynamics of individual CNTs, which reorient to form bundles. A mesoscale and an adaptive mesoscale model which discretise CNTs into series of nodes are developed and compared with atomistic simulations. These models account for relevant dynamic parameters, such as CNT bending stiffness and intermolecular attraction. The bundling time is found for individual CNTs of varying lengths and initial collision angles, in order to determine the bundle formation process resulting from individual CNT-CNT collision. The resulting bundling times are compared to CNT collision times, as the relative timescales determine the onset of aerogel formation. The adaptive mesoscale model can be applied to other one-dimensional high-aspect-ratio materials, such as boron nitride nanotubes or metallic nanowires, thus is of more general interest than solely for CNT applications.
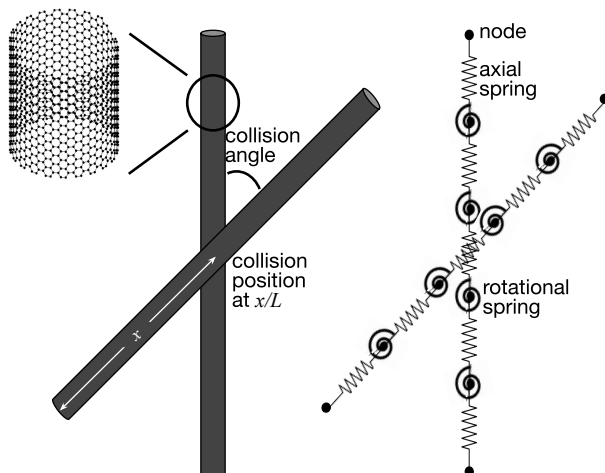
Figure 2: Illustration of initial CNT geometry with two CNTs at a specified collision position and angle. The CNTs are separated into cylindrical segments and each segment is represented by a node in the mesoscale model. The nodes are connected with massless axial and rotational springs.

Methods

Bundling Dynamics — Mesoscale Model

Derivation of Model Parameters

Here we present our method for deriving the relevant parameters for the mesoscale simulation, drawing on the methods developed by Buehler[24] and Volkov, Zhigilei et al.[25,26] The newly-defined method allows for adaptive modelling of the CNT interaction with higher particle resolution at the interface between CNTs and lower resolution at locations that are far from the advancing interface.

Node Mass

As shown in Figure 2, each molecule is treated as a series of nodes in the mesoscale model. The CNT is separated into cylindrical segments with the nodes sitting at a junction between two segments. The mass in the mesoscale model is concentrated only at the nodes and is evaluated as half the mass of the two segments that are attached to the node.[27] The axial

and rotational springs are massless.

Axial Stiffness

The axial stiffness of the CNT is represented with Hookean springs between consecutive nodes. The axial stiffness can be calculated with the assumption that the CNT is an elastic rod in tension and compression. Axial deformation is therefore associated with potential energy:

$$V_{\text{ax}} = k_r \Delta r^2 \tag{1}$$

with stiffness k_r given by:

$$k_r = \frac{1}{2} \frac{EA}{r_o} \tag{2}$$

where E is the CNT Young's Modulus, A is the cross-sectional area, r_o is the natural node spacing and Δr is the dynamically measured displacement from the natural node spacing. E is chosen as 1 TPa, which is appropriate for individual nanotubes[28] and A is calculated by treating one nanotube as a concentric graphene tube with radius R_{CNT} and wall thickness $d_{\text{G}} = 3.35\,\text{Å}$[29] with the following equation:

$$A = \pi \left[R_{\text{CNT}}^2 - (R_{\text{CNT}} - d_{\text{G}})^2 \right]. \tag{3}$$

Bending Stiffness

The bending stiffness is represented with Hookean rotational springs at each node. The assumption that a CNT behaves like an Euler beam is made.[30] Bending deformation is associated with potential energy:

$$V_{\text{rot}} = k_\theta \Delta\theta^2 \tag{4}$$

with bending stiffness k_θ given by:

$$k_\theta = \frac{1}{2} \frac{EI_A}{r_o} \tag{5}$$

where I_A is the second moment of area of the cross-section which can be computed as:

$$I_A = \frac{\pi}{4} \left[R_{\mathrm{CNT}}^4 - (R_{\mathrm{CNT}} - d_{\mathrm{G}})^4 \right].$$ (6)

Existing CNT and polymer bead-spring models use regularly spaced beads, in which r_o is equal to the bead spacing. This work expands this result to irregularly spaced beads or nodes, which are necessary for the adaptive mesoscale model, explained later in this section. In the adaptive modeling case, r_o takes the average value of the two node spacings on either side of the considered node. We determined this result by equating the bending potential energy of an Euler beam of length L and angle of curvature ϕ and the bending potential energy of a series of three nodes connected with two rigid links of total length L and bending angle $\Delta\theta$ (from eq. (4)).

Intermolecular Forces

A mesoscopic Lennard-Jones (LJ) potential based on the work by Volkov[26] is used to model the intermolecular vdW interactions between cylindrical CNT segments. The potential is based on the assumption that the carbon atoms of two CNT segments interact via a 12-6 Lennard-Jones[31] potential density of the form:

$$v_{\mathrm{LJ}} = \frac{4\epsilon}{n_{\mathrm{C}}^2} \left[\left(\frac{\sigma}{r} \right)^{12} - \left(\frac{\sigma}{r} \right)^6 \right],$$ (7)

where ϵ is an energy term, σ is a distance term and n_{C} is the surface number density of carbon atoms. The parameter r denotes the distance between two surface elements in the corresponding CNT segments. The interaction energy of two CNT segments is then given by:

$$V_{\mathrm{LJ}} = \iint\limits_{\mathcal{S}_1 \mathcal{S}_2} \mathrm{d}S_1 \mathrm{d}S_2 v_{\mathrm{LJ}},$$ (8)

where $\mathcal{S}_1, \mathcal{S}_2$ denote the respective CNT surfaces. This expression corresponds to a quadruple integral. Volkov and Zhigilei[26] applied a series of approximations to accelerate the evaluation of the interaction potential such that it can be efficiently used for computer simulations. They provide optimised expressions for armchair single-walled CNTs (SWCNTs) with chiral vectors of the form $\mathbf{c}_H = (n, n)$ where n is an integer between 5 and 20. For the full expressions of the approximated potential and implementation details, the reader is referred to the work of the original authors.[25,26]

Numerical Implementation

The simulation is performed in the canonical ensemble in a box with fixed boundaries. A Verlet integration algorithm[32] is used to time-march and obtain the trajectory of the nodes. A Nosé-Hoover thermostat chain[33] of length three is used to ensure rapid thermal equilibration of the simulation at all times. Specifically, the thermostat replaces the missing internal degrees of freedom of the CNT as a heat sink. The velocity of the particles is initialised to match the temperature of the surrounding gas which is implicitly modelled via the thermostat. The CNTs are initially placed such that their minimum separation is equal to the equilibrium distance of two parallel CNTs.

The model is implemented using the massively parallel software package LAMMPS,[34] which initializes the simulation according to the defined parameters and time-marches, while outputting the state at different time steps. The simulations were performed on the CSD3 supercomputer at the University of Cambridge.

Adaptive Mesoscale Model

In existing CNT mesoscale modeling work, a uniform particle placement is used. The equilibrium distance between adjacent nodes is the same as[24] or close to[25] the CNT diameter. Increasing the spacing does affect the intermolecular forces as the straight cylinder approximation deviates too far from a smooth curve. If two CNTs are parallel however, the potential

becomes invariant under translation along the respective CNT axes.[26] Therefore, changing the spacing of the nodes will have a vanishing effect on the computed intermolecular forces once CNTs have aligned. The accuracy reduces significantly however when the spacing is uniformly increased for all nodes. Indeed, early simulations confirmed that sparse node placement leads to large overestimates in the bundling time.

The problem with uniform fine spacing is the large computational cost associated with longer CNTs. Calculation time for each time step scales with the number of nodes and more significantly with the number of nodes for which an intermolecular potential is to be calculated. In addition, longer CNTs require more time to bundle, thus simulations with longer molecules require more time steps. This leads to traditional bead-spring simulations becoming too costly to model (simulations longer than years) for longer CNTs ($L_{\mathrm{CNT}} > 10\,\mu\mathrm{m}$).

We propose an adaptive mesoscale model, which uses a significantly reduced number of nodes and a spatially varying node resolution to capture the bundling dynamics accurately. We place a greater number of nodes where intermolecular forces are causing an attraction between the two chains and fewer nodes in the sections of chains that are spatially isolated. In addition, we also use fewer nodes for the sections of the chains that have formed a bundle. These sections tend to remain static over the course of the simulation and do not greatly affect the bundling dynamics, thus allowing for a lower resolution. We choose to employ three different node spacings with each spacing increasing by a factor of two from the previous spacing. The node spacing is adapted during the simulation to reduce the overall number of nodes that needs to be simulated. A smoother transition from a fine to a coarse resolution is employed to conserve system dynamics.

Determining Node Spacings

We denote the position of a node j in CNT i as $\mathbf{r}_{i,j}$. In our case, $i = 1, 2$; the method also fully generalises to arbitrary numbers of CNTs where i can correspondingly take larger

values. Node spacings are now indirectly determined by the CNT length associated with each node, which we will call the node size $l_{i,j}$. Node sizes and the spacing between two consecutive nodes $r_{0,i,j}$ are related as follows:

$$r_{0,i,j} = \frac{1}{2}(l_{i,j} + l_{i+1,j}).\tag{9}$$

We first find the minimum distance between node i, j and all nodes in the other CNT. This distance $\bar{d}$ can be formally written as:

$$\bar{d}(\mathbf{r}_{i,j}) = \min_{k \neq i,l} \{||\mathbf{r}_{i,j} - \mathbf{r}_{k,l}||\},\tag{10}$$

where $||\cdot||$ refers to the Euclidean norm. The actual node sizes $l_{i,j}$ are chosen from a list of preset values L_i which are linked to M distance ranges. These ranges are defined before the simulation by the end points of each range $\{d_0, \ldots, d_{M-2}\}$. This suffices to determine the node sizes for non-bundled CNTs. To re-coarsen CNTs once they are bundled, we define another threshold d_{CG} below which a node is marked for coarsening. In this case, the distance to determine the node size is the approximate minimum distance along the CNT of the considered node to the closest node which has not been marked for coarsening. We denote this distance by $\tilde{d}(r)$ and formally define:

$$\tilde{d}(\mathbf{r}_{i,j}) = \min\left\{\tilde{d}_-(\mathbf{r}_{i,j}), \tilde{d}_+(\mathbf{r}_{i,j})\right\},\tag{11}$$

where the previously described distance up and down the chain are given by:

$$\tilde{d}_+(\mathbf{r}_{i,j}) = \max_{k \neq j}\left\{\sum_{l=j+1}^{k} ||\mathbf{r}_{i,l-1} - \mathbf{r}_{i,l}|| \ \middle| \ \bar{d}(\mathbf{r}_{i,l}) < d_{\mathrm{CG}}, \ j+1 \leq l \leq k\right\},\tag{12}$$

$$\tilde{d}_-(\mathbf{r}_{i,j}) = \max_{k \neq j}\left\{\sum_{l=k+1}^{j} ||\mathbf{r}_{i,l-1} - \mathbf{r}_{i,l}|| \ \middle| \ \bar{d}(\mathbf{r}_{i,l}) < d_{\mathrm{CG}}, \ k+1 \leq l \leq j\right\},\tag{13}$$

respectively. This definition also takes into account the existence of chain ends which results in the refinement of the ends. If one does not desire to always refine the CNT ends, the distances $\tilde{d}_+(\mathbf{r}_{i,j})$ and $\tilde{d}_-(\mathbf{r}_{i,j})$ can be set to infinity if the respective chain end is reached in the sum. In this work however, we chose to refine CNT ends in order to maintain the correct CNT length throughout the simulation. We switch between the two defined distance measures based on the distance defined in eq. (10) according to:

$$d(\mathbf{r}_{i,j}) = \begin{cases} \overline{d}(\mathbf{r}_{i,j}), & \text{if } \overline{d}(\mathbf{r}_{i,j}) \geq d_{\mathrm{CG}}, \\ \tilde{d}(\mathbf{r}_{i,j}), & \text{else.} \end{cases} \tag{14}$$

The particle size $l_{i,j}$ is then determined by:

$$l_{i,j} = \begin{cases} L_0, & \text{if } 0 < d(\mathbf{r}_{i,j}) \leq d_0, \\ L_k, & \text{if } d_{k-1} < d(\mathbf{r}_{i,j}) \leq d_k, \\ L_{M-1}, & \text{if } d(\mathbf{r}_{i,j}) > d_{M-2}. \end{cases} \tag{15}$$

Cell Indexing

Practically, determining the distance $\overline{d}(\mathbf{r}_{i,j})$ requires computing the distances between all nodes in the system which scales quadratically in the number of nodes. This problem can be alleviated by using cell indexing.[35] In this method, the CNT structure is placed on a grid with spacing $b = d_{M-2}$ and the individual nodes are then sorted into cells on this grid. By construction of the grid, only distances between neighbouring cells need to be computed. If no nodes are found in the neighbouring cells then the computed distance defaults to being greater than d_{M-2}. With cell indexing, the number of distance computations scales linearly instead of quadratically.[35] The steps to determine the node sizes can then be summarised as follows:

1. Perform cell indexing for all CNTs in the structure.

2. Compute the distance $\overline{d}(\mathbf{r}_{i,j})$ for all nodes in the system by considering pairwise distances of nodes in neighbouring cells.

3. For nodes with $\overline{d}(\mathbf{r}_{i,j}) < d_{\mathrm{CG}}$, compute the distances $\tilde{d}_+(\mathbf{r}_{i,j})$ and $\tilde{d}_-(\mathbf{r}_{i,j})$. Starting at node j, iterate up the chain until a particle k with $\overline{d}(\mathbf{r}_{i,j}) \geq d_{\mathrm{CG}}$ or the end of the chain is reached. Whilst iterating, add the distances between two consecutive nodes to $\tilde{d}_+(\mathbf{r}_{i,j})$. Repeat the same procedure with iterating down the chain to compute $\tilde{d}_-(\mathbf{r}_{i,j})$ and choose the minimum to obtain $\tilde{d}(\mathbf{r}_{i,j})$.

4. Set the final distance $d(\mathbf{r}_{i,j})$ according to eq. (14).

5. Choose the node size by finding the correct distance bin using the rule described in eq. (15).

6. Compute the spacing between two neighbouring nodes using eq. (9).

This method has the benefit of being history independent and can also be readily parallelised with MPI by splitting the distance computation in the second step of the algorithm across multiple processes and choosing the minimum over all processes.

Adaptive Structure Regeneration

The node sizes can be dynamically adjusted over the course of the simulation. This occurs when the previous coarse-graining level does not match the predicted coarse-graining level based on the distance calculation described in the previous section. Nodes sizes are coarsened by combining several smaller nodes and placing a new node in the previous centre of mass. This approximation is sufficient as particles are usually coarsened either at the start of the simulation or once bundling and alignment have occurred. In both cases, the CNTs tend to be straight and the nodes will be close to their equilibrium positions. Inversely, node sizes are refined by evenly filling the available space occupied by the coarse nodes between the previous and next node within the chain. We found that linear interpolation

of the node positions works best. Attempts to use cubic spline interpolation led to violated energy conservation as new nodes were placed off-centre, increasing the potential energy of the system. Furthermore, the new velocities of the regenerated nodes are chosen such that linear momentum is conserved. The choice of velocity is unique during coarsening, whereas during refinement all refined nodes are chosen to have the same velocity. Conserving linear momentum during adaptive coarse-graining was found to be key to qualitatively and quantitatively preserve the dynamics of the simulation. The adaptive structure regeneration method is visualised with an example simulation of two 1 μm CNTs at a collision angle of 20° in Figure 3. By considering the nodes as point particles, it is possible to apply standard MD
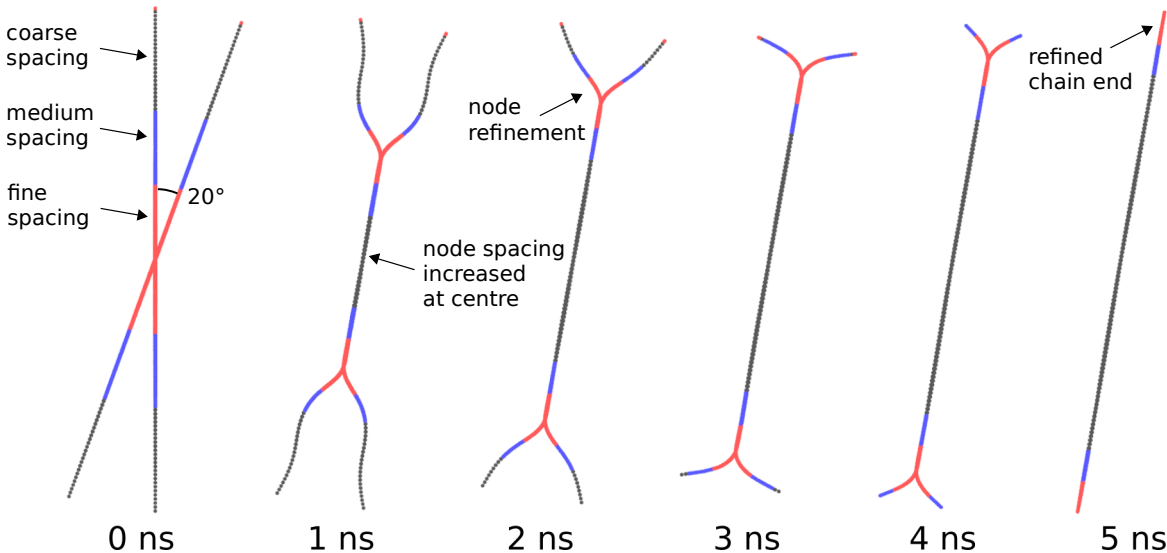
Figure 3: Time progression for a mesoscale simulation of two 1 μm CNTs at a collision angle of 20°. Individual points represent nodes in the mesoscale model. Coarse (black), medium (blue) and fine (red) node spacings were used. Annotations describe the adaptive structure regeneration method. Visualisation in VMD.[36]

methodology do measure thermodynamic quantities. Instantaneous temperature is computed based on the equipartition theorem[33] while the stress tensor can be calculated using the tensor-valued virial theorem[37]. The deformation energy can be instantaneously computed based on the position of the nodes as described by eqs. (1) and (2). While the number of nodes as well as node positions change during structure regeneration, the previously mentioned quantities are not strictly conserved. However, we found that the discontinuities

arising from the adaptive mesoscale model do not exceed the order of thermal fluctuations.

Atomistic Model

In order to validate the mesoscale model, we employed atomistic molecular dynamics simulations to simulate short SWCNTs. We used the Adaptive Intermolecular Reactive Empirical Bond Order (AIREBO) potential[38] to describe the forcefield of the system with two CNTs, where the short-range interaction is derived from the Reactive Empirical Bond Order (REBO) Potential[39] and the longer-range interaction is charaterised by a Lennard-Jones potential with a cut-off distance of $10.2\,\text{Å}$. The system is initialised such that the simulation begins at the starting point of the bundling process. Hence, we set the shortest distance between two CNT molecules to $3.5\,\text{Å}$, slightly more than the standard equilibrium distance of C-C in AIREBO potential which is $3.4\,\text{Å}$. After performing an energy minimization on the system, a simulation is performed in the canonical ensemble where the same Nosé-Hoover thermostat chain is used as in the mesoscale model. The time step is chosen as $2\,\text{fs}$.

Bundling Characterisation

A natural way to characterise the degree of bundling is to consider the intermolecular energy due to vdW interactions. Bundling occurs due to the tendency of the system to minimise its intermolecular potential energy. This energy should therefore decrease during a simulation, reaching a clearly defined minimum once bundling has finished. For the mesoscopic CNT potential employed in the presented model, two bundled CNTs can be assumed to be parallel. Girifalco et al.[40] have computed the adhesion energy per unit length of two infinitely long parallel CNTs to be:

$$E_{\text{adh}}/\text{Å} = \left(0.0378\sqrt{R_{\text{CNT}}/\text{Å}} - 3.13 \times 10^{-3}\right)\text{eV}/\text{Å}. \tag{16}$$

The adhesion energy provides a theoretical lower limit for the intermolecular energy of two bundled CNTs. The actual adhesion energy can then be determined by multiplying the value given by eq. (16) by the length over which two CNTs form a bundle. This value corresponds to the minimum intermolecular energy after bundle formation for 500 nm and longer CNTs. Shorter CNTs demonstrate finite length effects and the minimum of the intermolecular energy obtained during the simulation can be used. We can then define a bundling parameter β as the ratio of the instantaneous interaction energy and the minimum interaction energy of the system. We define the bundling time τ_B as the time at which β reaches 0.95.

Simulation Parameters

Unless stated otherwise, the parameters used in LAMMPS simulations are presented in Table 1. They are based on experimental observation, the setup of the FCCVD process and derivations described in this work. The effect of the choice of time step, thermostat relaxation time, minimum node spacing and coarse-graining parameters were studied to determine suitable values for the simulations. Adaptive coarse-graining was not considered while studying the first three parameters. The effect of the time step on bundling times was studied in a system of two 500 nm CNTs at a collision angle of 20°. For different time step values, the resulting intermolecular energy curves are shown in Figure 4a where a strong dependence of the bundling time on the time step can be observed. Indeed, Figure 4b shows that bundling time decreases with smaller time step and converges as the time step goes to zero, justifying our choice of 0.2 fs. Furthermore, the relaxation time τ_NH of the Nosé-Hoover thermostat was found to have no measurable effect on bundling dynamics.

Similarly, we considered two 200 nm CNTs at a collision angle of 20° and varied the minimum node size. Two different regimes can be observed in the energy curves and resulting bundling times shown in Figures 5a and 5b respectively. For large node sizes, bundling is nearly discrete as large segments suddenly come into range of the intermolecular force
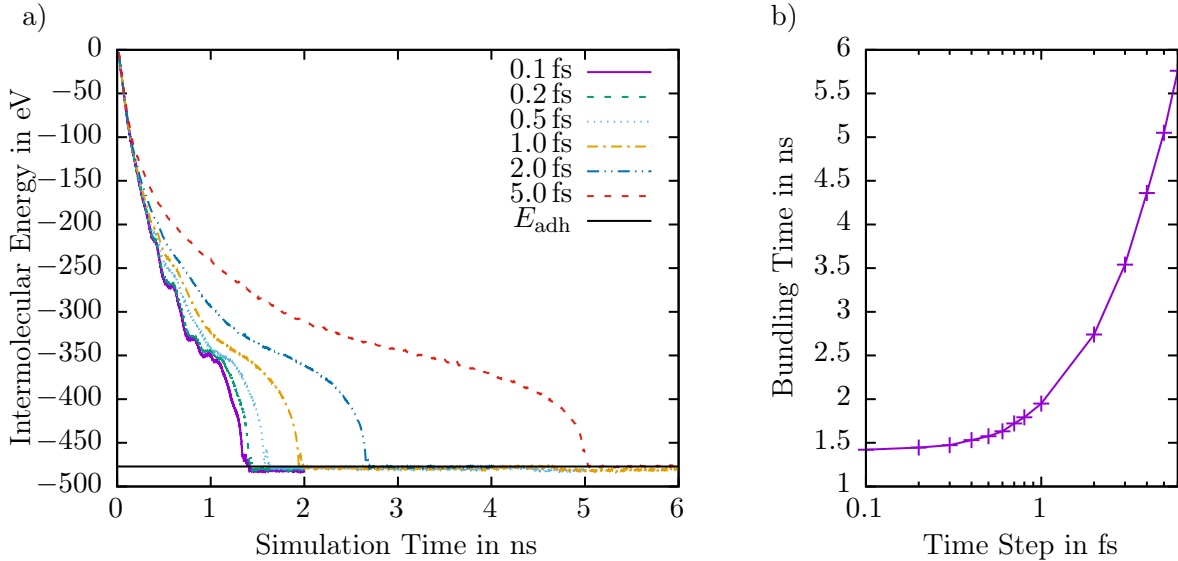
Figure 4: (a) Intermolecular energy versus simulation time for different time steps. (b) Bundling time versus logarithmic time step. Simulations were performed for two $500\,\text{nm}$ CNTs at a collision angle of $20°$ with a node spacing of $2\,\text{nm}$.

field. Decreasing the segment length also accelerates bundling as the inertia of individual segments decreases. Bundling times then visibly plateau before they enter a second regime where bundling times are significantly lower compared to the first regime. This regime is characterised by correctly resolving wave reflections in the CNTs which has previously been reported in the literature for a segment size of $1\,\text{nm}$.[27] Waves are induced by the release of deformation potential energy and reflected by the CNT ends, causing bundling to reverse once the reflected wave hits the CNT intersection. This can be observed by an increase in intermolecular energy, thus delaying the bundling process. As segment sizes decrease further below $3\,\text{nm}$, bundling times begin to increase again. We suspect this is due to an overestimation of attractive forces for smaller segments as the mesoscale approximation begins to break down. In turn, this leads to stronger attractions which inhibit the reversal of bundling. Nevertheless, we choose $2\,\text{nm}$ as the minimum node spacing as it ensures reasonable simulation times while still resolving wave reflections. This choice also agrees with the original segment size employed by Volkov et al.[25] We further note that decreasing

18

segment sizes lead to a lower final adhesion energy. We theorise this is due to finite size effects of the segments preventing perfect parallel alignment. Small deviations in the relative angle can then significantly decrease the adhesion energy. For our final choice of 2 nm however, the adhesion energy is in good agreement with the theoretical value provided in eq. (16) as can be seen in Figure 4a.
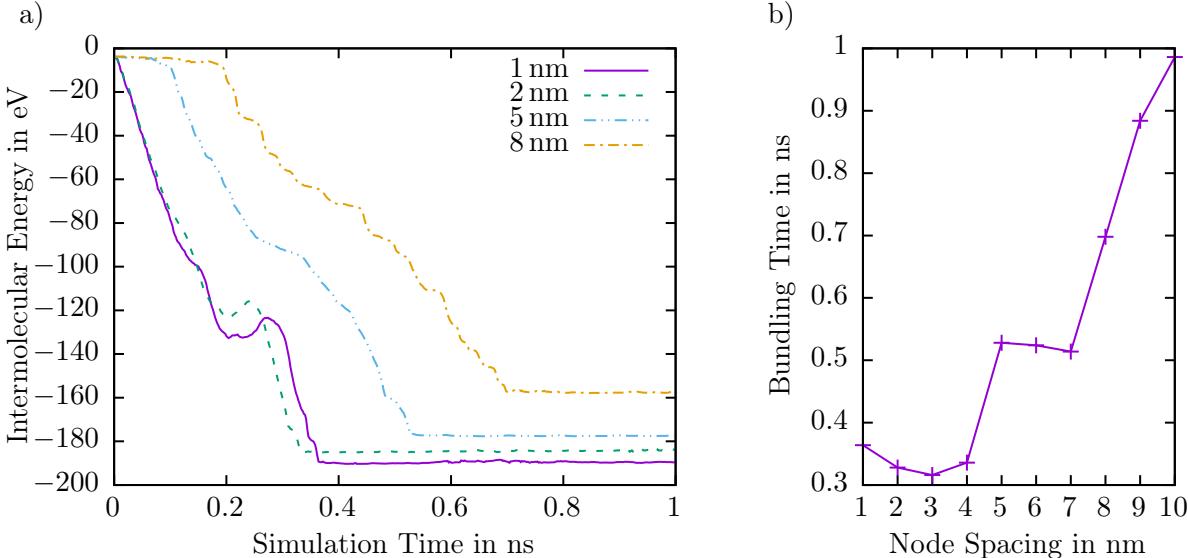

Figure 5: (a) Intermolecular energy versus simulation time for different node spacings. (b) Bundling time versus node spacing. Simulations were performed for two 200 nm CNTs at a collision angle of 20°.

Results and Discussion

The simulation methods used are compared in figure 6. The mesoscale model is compared with an atomistic simulation of SWCNTs, also performed with LAMMPS, in Figure 6a. The simulation results for the atomistic and mesoscale model are also visualised in Figures 7a and 7b respectively. The potential energy of the system decreases with time as the two CNTs bundle and their intermolecular energy decreases. The reduction in intermolecular energy takes longer for larger collision angles between the CNTs. Timescales for bundling are of the order 0.1 to 1 ns for both simulations. While the results for both models agree very well for

Table 1: Parameters used in LAMMPS simulations.

Parameter	Symbol	Value
Chiral vector	$\mathbf{c}_{\mathrm{h}}$	(10,10)
CNT radius	R_{CNT}	6.79 Å
Effective CNT wall thickness	d_{G}	3.35 Å
Fine node spacing	L_0	20.0 Å
Medium node spacing	L_1	40.0 Å
Coarse node spacing	L_2	80.0 Å
Coarsening threshold	d_{CG}	60.0 Å
Fine spacing threshold	d_0	500.0 Å
Medium spacing threshold	d_1	1000.0 Å
Temperature	T	1200.0 K
Time step	dt	0.2 fs
Nosé-Hoover relaxation time	τ_{NH}	10.0 fs
Young's Modulus	E	1.0 TPa
Mass per unit length	m'	195.17 u Å^{-1}
Fine axial spring stiffness	k_r	268.90 N m^{-1}
Fine rotational spring stiffness	k_θ	290.62 eV rad^{-1}

small collision angles, they begin to deviate for angles above 20°. The atomistic model also drops to a lower final intermolecular energy compared to the mesoscopic model.

We theorise that the atomistic model leads to faster bundling as the CNTs can deform along the diameter, deviating from the perfect cylindrical shape assumed by the mesoscopic model.[26] Hence, the interface between the two bundled CNTs has a greater area, leading to stronger attraction and a greater adhesion energy. The bending stiffness computed based on Euler beam theory as listed in Table 1 is about 50 % lower than the value reported for atomistic simulations[27]. However, this reported value is only valid for perfectly cylindrical CNTs. Since the deformation after alignment leads to a decreased width of the CNT along the bending axis and the second moment of area scales cubically in said width, the bending stiffness should also decrease significantly. In turn, the weak attractions have to overcome a reduced stiffness, therefore leading to accelerated bundling. We further note that the stretching stiffness provided in Table 1is approximately 14 %lower than the corresponding value for the atomistic model[27]and should therefore not cause any significant differences in
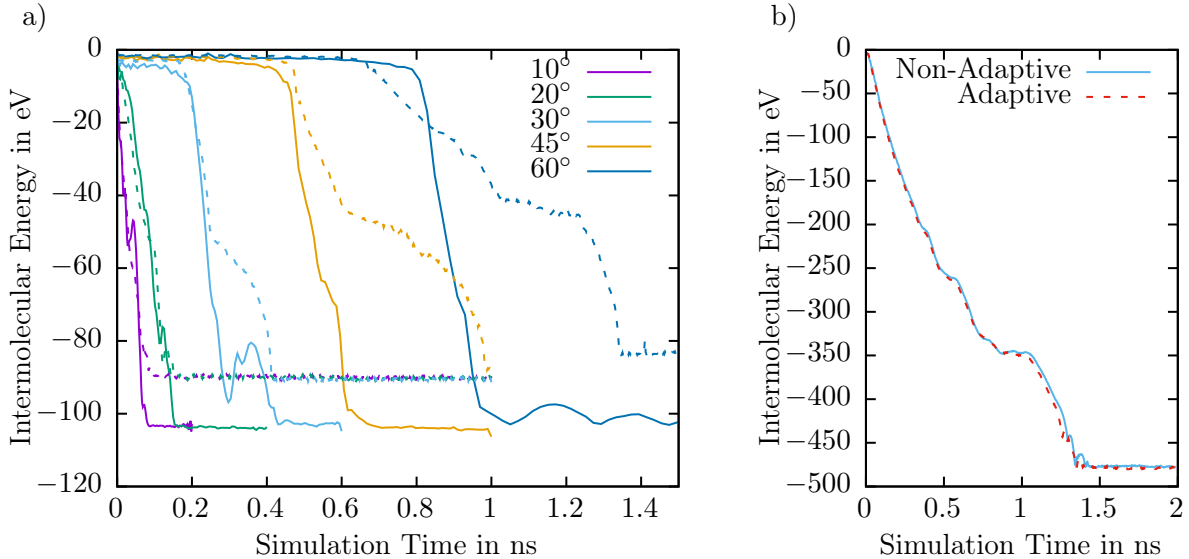
Figure 6: (a) Intermolecular bundling energy of 100 nm SWCNTs at different collision angles, predicted by atomistic (solid lines) and mesoscale (dashed lines) simulations shown for different collision angles. (b) Comparison of the adaptive mesoscale model with the non-adaptive mesoscale simulation with uniformly placed nodes. The simulations were performed for 500 nm CNTs at 20°.

bundling behaviour.

The adaptive mesoscale model is compared with the non-adaptive mesoscale model in Figure 6b. The reduction in intermolecular energy for both cases follows nearly the same trajectory. While the resulting bundling times of both models are within 1.5 %, the computational run time for the adaptive mesoscale model was 46 % of the non-adaptive case. We found that computational speed-up increases with increasing CNT length. For the bundling of two 10 μm CNTs, we obtained a speed-up of nearly five times compared to the non-adaptive model. The adaptive mesoscale model thus allows the simulation of CNTs in the μm order. Results for CNTs whose length is equal to or longer than 500 nm are henceforth obtained with the adaptive method unless stated otherwise.

The agreement of the time evolution trend for CNT intermolecular energy during bundling validates the use of the mesoscale and the adaptive mesoscale models for bundling simulations. The models are designed to capture structural effects and intermolecular interactions,
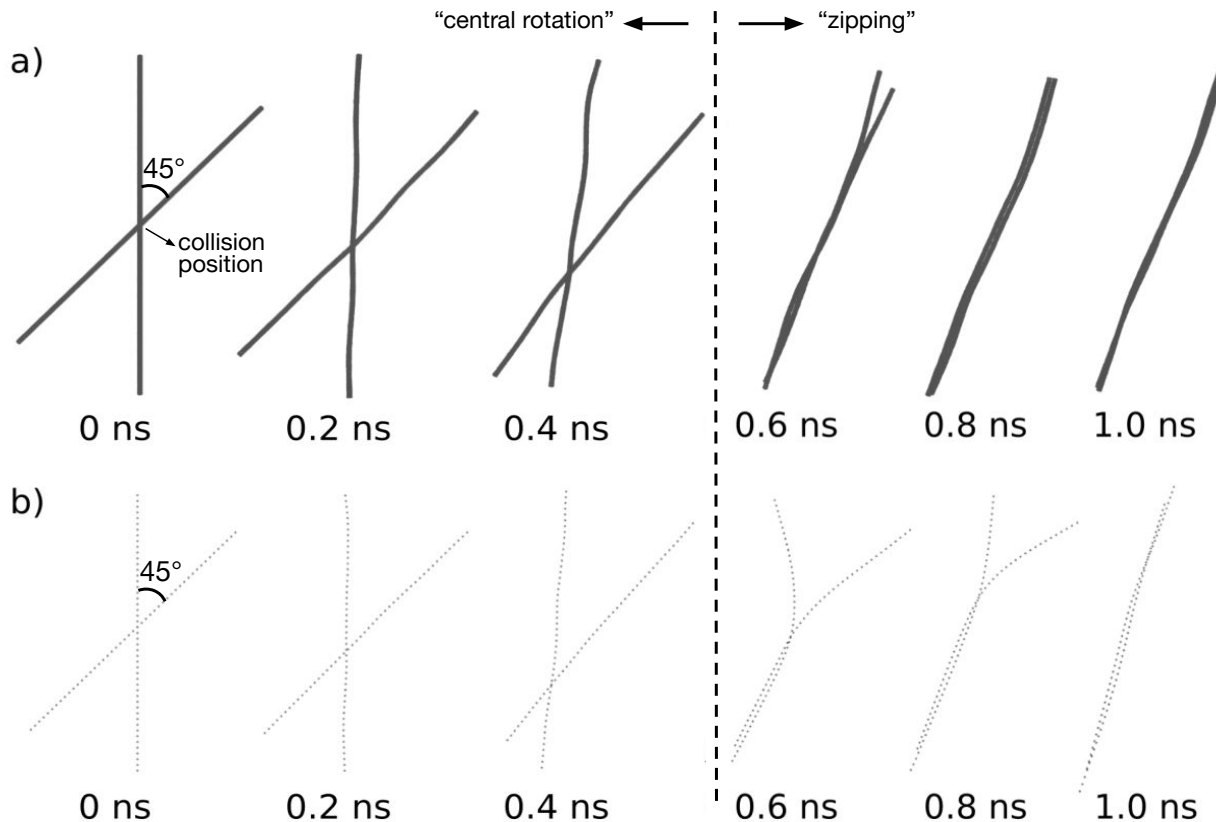
Figure 7: (a) Simulation progression of atomistic CNT bundling for two 100 nm SWCNTs at 45°. (b) Simulation progression of mesoscale CNT bundling for two 100 nm SWCNTs at 45°. Points represent the individual nodes in the model, dashed line and arrows with annotations indicate where the system transitions from the central rotation to the zipping regime. Visualisation in VMD.[36]

which allow the efficient simulation of CNT bundling.

Figure 8 shows the bundling of CNTs of different lengths at different collision angles. As expected, smaller collision angles result in faster bundling, as vdW forces are stronger and the CNTs have to travel a shorter distance overall.

In general, the motion of the CNTs can be divided into two regimes. Initially, the centres of the CNTs rotate and approach each other, as seen in Figures 7a and 7b for the first 0.4 ns. During this "central rotation", no significant bending of the CNTs can be seen. However, one does observe a drift in the collision position and a decrease in the relative angle between the CNTs. This is accompanied by the bundling parameter of the arrangement staying close to zero and only increasing slowly which can be seen for the 45° case in Figure 8a up to

approximately 0.5 ns. This motion requires increasing amounts of time with increasing CNT length, as the vdW attraction has to overcome an increasing moment of inertia. Larger collision angles also extend this phase as the CNT ends have to travel a greater distance. After the centres have aligned, a bundle starts forming and the bundled region extends in a "zipping" motion. Here, neighbouring segments begin to align into a bundle and the bending stiffness of the CNT causes the entire chain to drift towards the effective bundle axis. For two 100 nm CNTs, the transition to the zipping regime occurs at about 0.5 ns, In Figures 7a and 7b, bending and zipping of the CNTs can be seen for simulation times greater than 0.4 ns which is accompanied by an abrupt change in the rate at which the bundling parameter increases in Figure 8a. The same transition can be seen in the later parts of figures 8a to d for collision angles greater than 30° when the bundling parameter suddenly starts to increase after visually remaining close to zero during the first 0.5–1.5 ns of the simulation. Another example of a mesoscale simulation in the zipping regime is also visualised in Figure 3. For small collision angles, the central rotation regime vanishes as the system is already initialised in a state where zipping can occur. With increasing collision angles however, the bundling behaviour is beginning to be dominated by central rotation. For a collision angle of 60°, CNTs of lengths starting at 500 nm do not enter the zipping regime in the simulated time. Likewise, for CNT lengths greater or equal to 2 µm, a collision angle of 45° is large enough for the system to remain in the central rotation regime in the considered time frame. In these cases, the bundling parameter remains well below 1 % over the course of the simulation. Therefore, Figure 8 only depicts the results of simulations where the CNTs did enter the zipping regime during the simulation. The results indicate that the collision angle both increases the duration of the central and zipping regimes.

The bundling of CNTs of dissimilar lengths is presented in Figure 9a. The intermolecular energy decreases to its minimum value in a very similar time interval (0.1 to 0.15 ns) for all lengths. When the one CNT is longer than the other CNT, the bundling time is effectively only a function of the shorter CNT length. For 20°, the CNTs are already in the zipping

regime, thus the segments quickly align regardless of the length of the longer CNT. Due to its greater inertia, the long CNT remains almost stationary, while the short CNT reorients itself to become parallel with the long CNT. For the 100 nm–100 nm pair, one observes a short "dip" in the bundling parameter after initially reaching unity in Figure 9a. This can be explained by the CNT ends undergoing an elastic collision, causing them to rebound. As CNT ends attract other CNTs more weakly than the interior of a CNT, this effect is only observed for the 100 nm–100 nm pair. In the other cases, the vdW attractions outweigh the inertia of the CNT ends and no rebound event can be seen in Figure 9a.

Figure 9b shows the evolution of bundling parameter for two 500 nm CNTs colliding at different positions at an angle of 20°. No clear trend for the bundling time with respect to the initial position can be observed within the simulation uncertainty. All bundling times are between 1.23 and 1.48 ns and therefore of the same order. We conclude the collision position has little effect on the bundling dynamics as the length over which the CNTs are finally bundled is nearly constant for all cases and only subject to statistical fluctuation.

Figure 10 summarises key results. The bundling time is obtained as explained in the Methods section, by determining the time at which the system approaches 95 % of the minimum intermolecular energy. Up to lengths of 1 μm, the final value is determined from the simulation results. For the longer CNTs, the theoretical value from eq. (16) is used. The results for 45° and 60° have fewer data points as bundling is dominated by central rotation for these angles. Above CNT lengths of 500 nm and 2 μm respectively, the CNTs did not leave the central rotation domain over the course of the simulation. Beginning at 2 μm CNTs at 20°, all subsequent bundling times have been estimated by linear extrapolation of the bundling parameter as a function of time. For the linear extrapolation, we used the last available nanosecond of simulation results. In all cases, the asymptotic standard error of the linear regression fit was less than 1 % of the obtained fitting parameters. As the bundling process tends to slow down with progressing simulation time as seen in Figures 8e and f, the linear extrapolation provides a conservative lower bound for the real bundling times.

As expected, we find that bundling times scale strongly with the length of bundling CNTs. Fitting a power law to the data obtained for the 30° case yields the following expression:

$$\tau_{\mathrm{B}}(L_{\mathrm{CNT}}) = 10^{-4.28\pm0.43} \times (L_{\mathrm{CNT}}/\mathrm{nm})^{1.80\pm0.14}\mathrm{ns}, \tag{17}$$

where the uncertainty terms give the asymptotic standard error.

In order to gain insight into aerosol formation, it is useful to compare the bundling times with CNT collision times. Using previously calculated collision kernels,[5] the characteristic collision time, τ_{col}, can be directly obtained from the collision kernel, β, and the number density, N, of CNTs in the system by the well-known relation,[41] $\tau_{col} = 2/(\beta N)$. For a number density of $N = 1 \times 10^{11}\,\mathrm{m}^{-3}$, 100 nm and 1 mm CNTs experience collision times of $\tau_{col} = 3 \times 10^3\,\mathrm{s}$ and $\tau_{col} = 4 \times 10^2\,\mathrm{s}$, respectively. At a number density equal to $N = 1 \times 10^{14}\,\mathrm{m}^{-3}$, the collision times are decreased by a factor of 1000, namely to $\tau_{col} = 3\,\mathrm{s}$ and $\tau_{col} = 0.3\,\mathrm{s}$, respectively. These collision times are much longer than the bundling times of Figure 10. Thus, the formation of bundles occurs almost immediately upon collision of the CNTs allowing for large bundles to form (up to 20 CNTs per bundle) before long-range aerogel structure is produced, which is consistent with TEM studies of the material as shown in Figure 1.

Conclusions

The adaptive mesoscale models predict how individual CNTs align to form bundles. Computational adaptivity allows the simulation of long CNTs, which would have been very computationally expensive with a non-adaptive approach. The adaptive mesoscale model can be applied to other one-dimensional materials.

The bundling simulation results give significant new insight in the aerogel formation process. The bundling of CNTs is manifested in two regimes. Initially, the centres of the CNTs rotate towards each other and reduce their intersection angle near the collision

location. This is described here as central rotation. When the intersection angle is small, the CNTs start forming a bundle. The central region of the CNTs forms the bundle and the bundled region expands towards the ends of the CNTs, which we refer to as zipping. The central rotation regime is attributed to large initial collision angles and vanishes for collision angles below 20°. For collision angles above 30°, central rotation begins to dominate the bundling process for CNTs longer than 1 µm. A higher collision angle increases bundling time by affecting both bundling regimes, namely central rotation and zipping. Its effect on central rotation appears to be more drastic, changing the bundling time by about one order of magnitude in the 100 and 200 nm cases and preventing longer CNTs to enter the zipping regime altogether for collision angles above 30°. Bundling time increases according to a power law of the CNT length, as both parts of the bundling mechanism take longer. The initial alignment phase takes longer due to the increased inertia presented by the long CNTs, and the second bundle growth phase needs more time as the bundle length is longer.

Collision position does not affect the bundling time and behaviour, as the overlapping chain length is the same for all collision positions. For collisions of CNTs of different lengths, bundling time is only a function of the short CNT length, as long as the second CNT is longer such that end-end interactions become negligible. We conclude that bundling dynamics are thus mainly determined by the length of the shorter CNT.

CNT bundling times are significantly faster than the characteristic collision time, thus CNTs form bundles at a fast rate after every collision. This explains the existence of bundles in the experimentally observed aerogel, as opposed to a network of individual CNTs.

Acknowledgement

References

(1) De Volder, M. F. L.; Tawfick, S. H.; Baughman, R. H.; Hart, A. J. Carbon Nanotubes: Present and Future Commercial Applications. *Science* **2013**, *339*, 535–539.

(2) Weller, L.; Smail, F. R.; Elliott, J. A.; Windle, A. H.; Boies, A. M.; Hochgreb, S. Mapping the Parameter Space for Direct-Spun Carbon Nanotube Aerogels. *Carbon* **2019**, *146*, 789–812.

(3) Gspann, T. S.; Smail, F. R.; Windle, A. H. Spinning of Carbon Nanotube Fibres Using the Floating Catalyst High Temperature Route: Purity Issues and the Critical Role of Sulphur. *Faraday Discuss.* **2014**, *173*, 47–65.

(4) Li, Y.-L.; Kinloch, I. A.; Windle, A. H. Direct Spinning of Carbon Nanotube Fibers from Chemical Vapor Deposition Synthesis. *Science* **2004**, *304*, 276–278.

(5) Boies, A. M.; Hoecker, C.; Bhalerao, A.; Kateris, N.; de La Verpilliere, J.; Graves, B.; Smail, F. Agglomeration Dynamics of 1D Materials: Gas-Phase Collision Rates of Nanotubes and Nanorods. *Small* **2019**, *15*, 1900520.

(6) Lushnikov, A.; Negin, A.; Pakhomov, A. Experimental Observation of the Aerosol-Aerogel Transition. *Chemical Physics Letters* **1990**, *175*, 138–142.

(7) Hou, G.; Ng, V.; Xu, C.; Zhang, L.; Zhang, G.; Shanov, V.; Mast, D.; Kim, W.; Schulz, M.; Liu, Y. et al. Multiscale Modeling of Carbon Nanotube Bundle Agglomeration inside a Gas Phase Pyrolysis Reactor. *MRS Advances* **2017**, *2*, 2621–2626.

(8) Smail, F.; Boies, A.; Windle, A. Direct Spinning of CNT Fibres: Past, Present and Future Scale Up. *Carbon* **2019**, *152*, 218–232.

(9) Hoecker, C.; Smail, F.; Bajada, M.; Pick, M.; Boies, A. Catalyst Nanoparticle Growth Dynamics and their Influence on Product Morphology in a CVD Process for Continuous Carbon Nanotube Synthesis. *Carbon* **2016**, *96*, 116–124.

(10) Hoecker, C.; Smail, F.; Pick, M.; Weller, L.; Boies, A. M. The Dependence of CNT Aerogel Synthesis on Sulfur-driven Catalyst Nucleation Processes and a Critical Catalyst Particle Mass Concentration. *Scientific Reports* **2017**, *7*, 14519.

(11) Hoecker, C.; Smail, F.; Pick, M.; Boies, A. The Influence of Carbon Source and Catalyst Nanoparticles on CVD Synthesis of CNT Aerogel. *Chemical Engineering Journal* **2017**, *314*, 388–395.

(12) Kim, K.-E.; Kim, K.-J.; Jung, W. S.; Bae, S. Y.; Park, J.; Choi, J.; Choo, J. Investigation on the Temperature-Dependent Growth Rate of Carbon Nanotubes Using Chemical Vapor Deposition of Ferrocene and Acetylene. *Chemical Physics Letters* **2005**, *401*, 459–464.

(13) Gopalakrishnan, R.; Thajudeen, T.; Hogan, C. J. Collision Limited Reaction Rates for Arbitrarily Shaped Particles across the Entire Diffusive Knudsen Number Range. *Journal of Chemical Physics* **2011**, *135*.

(14) Thajudeen, T.; Gopalakrishnan, R.; Hogan, C. J. The Collision Rate of Nonspherical Particles and Aggregates for All Diffusive Knudsen Numbers. *Aerosol Sci. Technol* **2012**, *46*, 1174–1186.

(15) Thajudeen, T.; Deshmukh, S.; Hogan, C. J. Langevin Simulation of Aggregate Formation in the Transition Regime. *Aerosol Science and Technology* **2015**, *49*, 115–125.

(16) Zhang, D.-B.; James, R. D.; Dumitrică, T. Electromechanical Characterization of Carbon Nanotubes in Torsion via Symmetry Adapted Tight-Binding Objective Molecular Dynamics. *Phys. Rev. B* **2009**, *80*, 115418.

(17) Han, Y.; Elliott, J. Molecular Dynamics Simulations of the Elastic Properties of Polymer/Carbon Nanotube Composites. *Computational Materials Science* **2007**, *39*, 315–323.

(18) Zhong, H.; Lukes, J. R. Interfacial Thermal Resistance between Carbon Nanotubes: Molecular Dynamics Simulations and Analytical Thermal Modeling. *Phys. Rev. B* **2006**, *74*, 125403.

(19) Zhang, C.; van Duin, A. C.; Seo, J. W.; Seveno, D. Weakening Effect of Nickel Catalyst Particles on the Mechanical Strength of the Carbon Nanotube/Carbon Fiber Junction. *Carbon* **2017**, *115*, 589–599.

(20) Jr., P. E. R. A Theory of the Linear Viscoelastic Properties of Dilute Solutions of Coiling Polymers. *The Journal of Chemical Physics* **1953**, *21*, 1272–1280.

(21) Somasi, M.; Khomami, B.; Woo, N. J.; Hur, J. S.; Shaqfeh, E. S. Brownian Dynamics Simulations of Bead-Rod and Bead-Spring Chains: Numerical Algorithms and Coarse-Graining Issues. *Journal of Non-Newtonian Fluid Mechanics* **2002**, *108*, 227–255, Numerical Methods Workshop S.I.

(22) Underhill, P. T.; Doyle, P. S. On the Coarse-Graining of Polymers into Bead-Spring Chains. *Journal of Non-Newtonian Fluid Mechanics* **2004**, *122*, 3–31.

(23) Maiti, A.; Wescott, J.; Kung, P. Nanotube–Polymer Composites: Insights from

Flory–Huggins Theory and Mesoscale Simulations. *Molecular Simulation* **2005**, *31*, 143–149.

(24) Buehler, M. J. Mesoscale Modeling of Mechanics of Carbon Nanotubes: Self-Assembly, Self-Folding, and Fracture. *Journal of Materials Research* **2006**, *21*, 2855–2869.

(25) Volkov, A.; R. Simov, K.; V. Zhigilei, L. Mesoscopic Model for Simulation of CNT-Based Materials. *ASME International Mechanical Engineering Congress and Exposition, Proceedings* **2008**, *13*, 1235–1245.

(26) Volkov, A. N.; Zhigilei, L. V. Mesoscopic Interaction Potential for Carbon Nanotubes of Arbitrary Length and Orientation. *The Journal of Physical Chemistry C* **2010**, *114*, 5513–5531.

(27) V. Zhigilei, L.; Wei, C.; Srivastava, D. Mesoscopic Model for Dynamic Simulations of Carbon Nanotubes. *Physical Review B* **2005**, *71*, 165417.

(28) Yu, M.-F.; Lourie, O.; Dyer, M. J.; Moloni, K.; Kelly, T. F.; Ruoff, R. S. Strength and Breaking Mechanism of Multiwalled Carbon Nanotubes Under Tensile Load. *Science* **2000**, *287*, 637–640.

(29) Peigney, A.; Laurent, C.; Flahaut, E.; Bacsa, R.; Rousset, A. Specific Surface Area of Carbon Nanotubes and Bundles of Carbon Nanotubes. *Carbon* **2001**, *39*, 507–514.

(30) Timoshenko, S. *History of Strength of Materials: With a Brief Account of the History of Theory of Elasticity and Theory of Structures*; Dover Civil and Mechanical Engineering Series; Dover Publications, 1953.

(31) Jones, J. E. On the Determination of Molecular Fields. II. From the Equation of State of a Gas. *Proceedings of the Royal Society of London Series A* **1924**, *106*, 463–477.

(32) Verlet, L. Computer "Experiments" on Classical Fluids. I. Thermodynamical Properties of Lennard-Jones Molecules. *Phys. Rev.* **1967**, *159*, 98–103.

(33) Frenkel, D.; Smit, B. *Understanding Molecular Simulation*, 2nd ed.; Academic Press: San Diego, 2002; pp 63–108, 139–164.

(34) Plimpton, S. Fast Parallel Algorithms for Short-Range Molecular Dynamics. *J. Comput. Phys.* **1995**, *117*, 1–19.

(35) Allen, M. P.; Tildesley, D. J. *Computer Simulation of Liquids*; Clarendon Press: New York, NY, USA, 1989.

(36) Humphrey, W.; Dalke, A.; Schulten, K. VMD – Visual Molecular Dynamics. *Journal of Molecular Graphics* **1996**, *14*, 33–38.

(37) Thompson, A. P.; Plimpton, S. J.; Mattson, W. General Formulation of Pressure and Stress Tensor for Arbitrary Many-Body Interaction Potentials Under Periodic Boundary Bonditions. *The Journal of Chemical Physics* **2009**, *131*, 154107.

(38) Stuart, S. J.; Tutein, A. B.; Harrison, J. A. A Reactive Potential for Hydrocarbons with Intermolecular Interactions. *The Journal of Chemical Physics* **2000**, *112*, 6472–6486.

(39) Brenner, D. W.; Shenderova, O. A.; Harrison, J. A.; Stuart, S. J.; Ni, B.; Sinnott, S. B. A Second-Generation Reactive Empirical Bond Order (REBO) Potential Energy Expression for Hydrocarbons. *Journal of Physics: Condensed Matter* **2002**, *14*, 783–802.

(40) Girifalco, L. A.; Hodak, M.; Lee, R. S. Carbon Nanotubes, Buckyballs, Ropes, and a Universal Graphitic Potential. *Phys. Rev. B* **2000**, *62*, 13104–13110.

(41) Friedlander, S.; Friedlander, P. *Smoke, Dust, and Haze: Fundamentals of Aerosol Dynamics*; Topics in Chemical Engineering: A Series of Textbooks and Monographs; Oxford University Press, 2000.
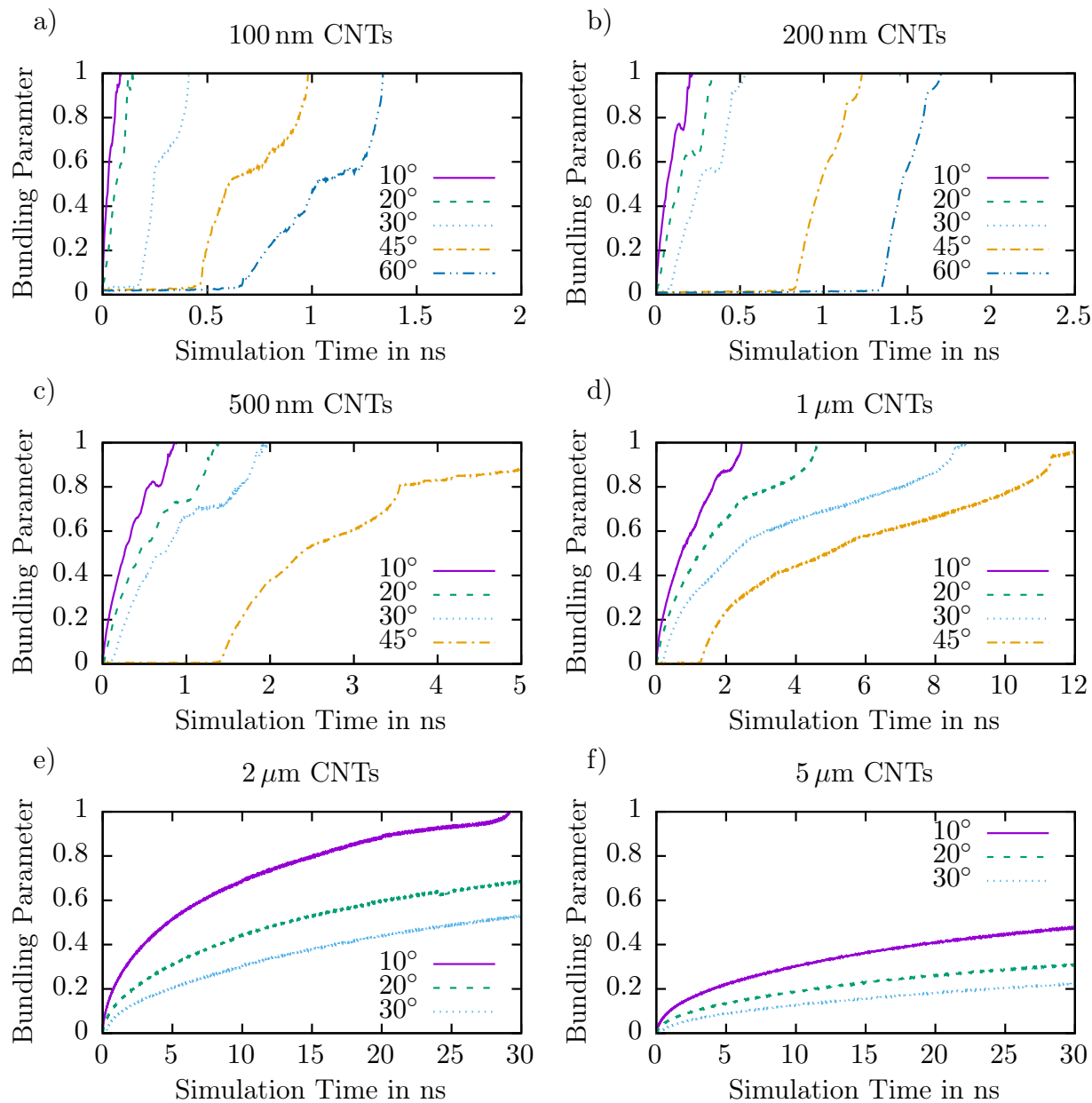
Figure 8: Bundling parameter, $\beta(t) = E(t)/E_{\mathrm{adh}}$, versus simulation time for different CNT lengths and at different collision angles.

a) 100 nm CNT

b) 500 nm CNTs
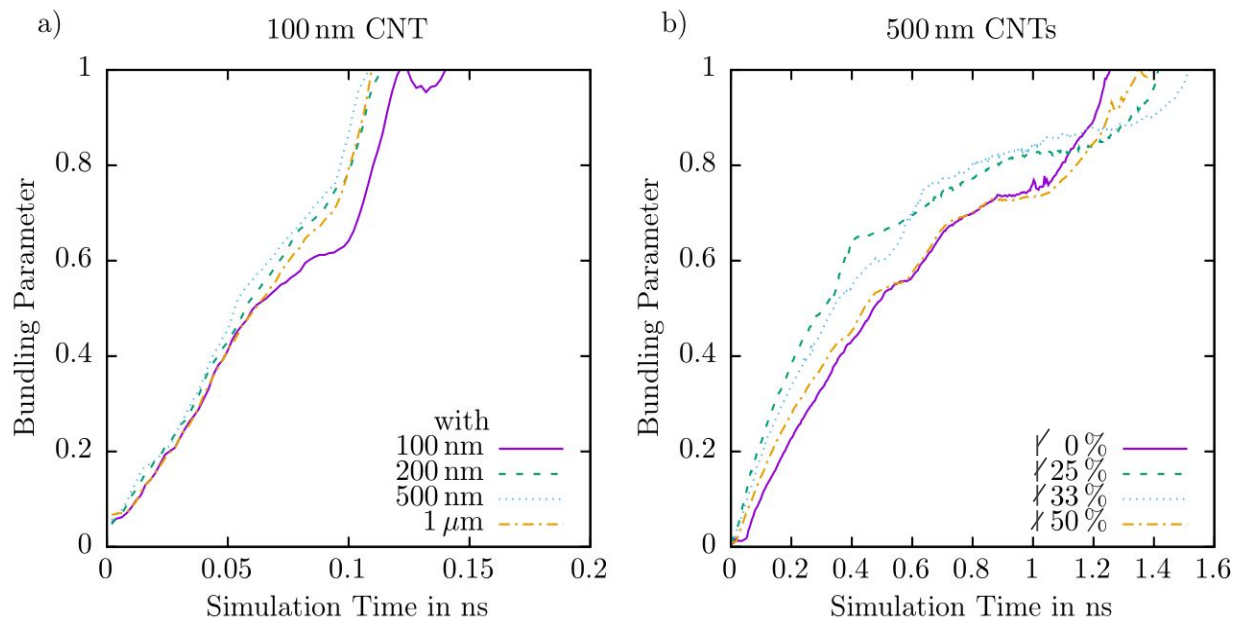
Figure 9: (a) Collision of a 100 nm CNT with other CNTs of different lengths at 20°. (b) Bundling of two 500 nm CNTs with different collision positions at 20°. Pictograms in the legend visualise the initial configurations at different collision positions.
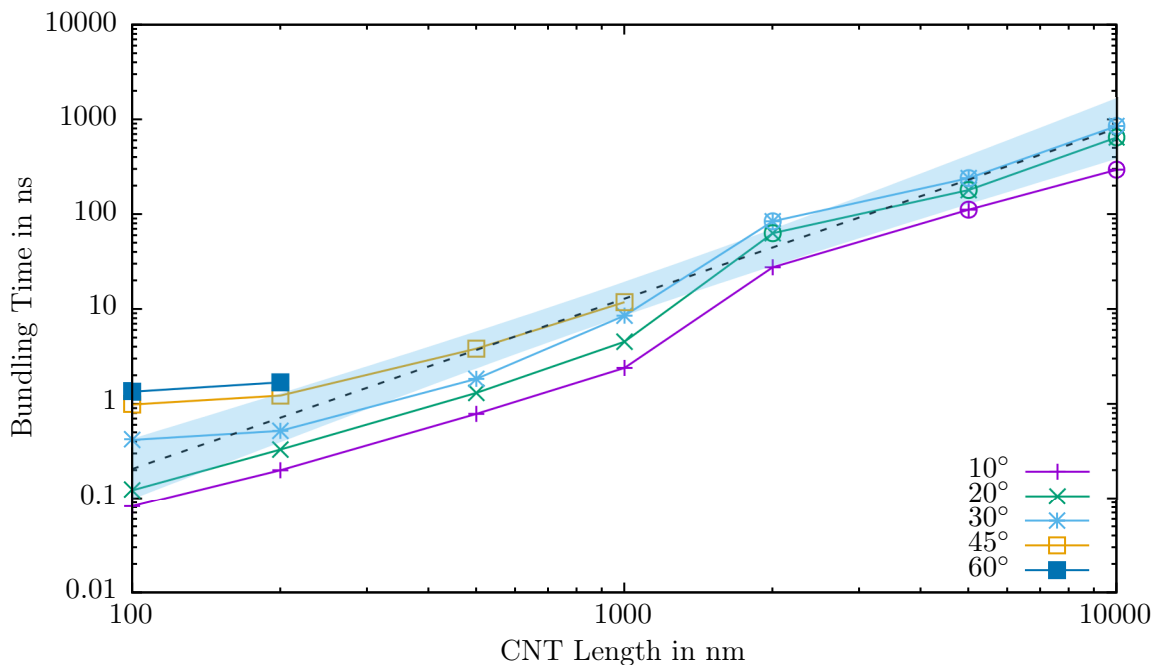

Figure 10: Log-log plot of bundling times versus CNT lengths for different collision angles. Circled points represent extrapolated values. The dashed line shows the power law fit from eq. 17 and the shaded area represents the 95 % confidence interval for the corresponding linear regression fit.

TOC Graphic